Biophysical Chemistry 24 (1986) 221–234
Elsevier

BPC 01072

DIELECTRIC BEHAVIOR OF POLYELECTROLYTES

IV. ELECTRIC POLARIZABILITY OF RIGID BIOPOLYMERS IN ELECTRIC FIELDS

Jeff A. ALTIG, Gary E. WESENBERG and Worth E. VAUGHAN

Department of Chemistry, University of Wisconsin-Madison, Madison, WI 53706, U.S.A.

Received 19th February 1986
Revised manuscript received 5th May 1986
Accepted 7th May 1986

Key words: Polyelectrolyte; Dielectric response; Electric polarizability; Kerr effect; Counterion interaction; DNA oligomer; Disk membrane vesicle

The equilibrium Kerr effect of a system of mobile charges constrained to the surface of biomacromolecules is calculated. Cylindrical and spherical geometries are considered. For the cylinder we determine the anisotropy of electric polarizability as a function of length, temperature, and number of charged species in the low-field regime, and the fraction of the maximum induced dipole in the field direction for higher electric fields. The results are compared to experimental data for DNA oligomers taken from the literature. With spherical geometry we calculate the fractional induced dipole moment as a function of electric field strength and from this deduce the orientation function. The field dependence of the orientation function is compared to experimental data in the literature for bovine disk membrane vesicles.

1. Introduction

The dynamics of protein motion on and equilibrium binding to natural polyelectrolytes intimately involves the small ions found in the vicinity of the biomacromolecule. A characterization of small ion interactions with the polyelectrolyte and with each other forms a component of the overall view of the mechanism of the protein dynamics. Thus, a model molecular picture of the small ion behavior provides a starting point for describing the equilibrium and dynamical properties of more complex biopolymer assemblies. The consensus view is that perturbation of the ionic atmosphere of the polyelectrolyte is the mechanism for the dielectric relaxation and the dynamic Kerr effect indicating the utility of applied electric fields as probes of the molecular equilibria and dynamics.

In previous work (papers I [1], II [2] and III [3] of this series) a model of a cylindrical polyelectrolyte with mobile surface charges subject to Coulomb forces was used to generate a prediction for the equilibrium and dynamic dielectric response. The intended application is the dielectric response of aqueous solutions of DNA oligomers; such data are not currently found in the literature. The dielectric response implies that only small external electric fields are present.

This work develops expressions for the magnitude of the equilibrium Kerr effect of rigid polyelectrolytes with constrained mobile charges interacting via the Coulomb potential. General expressions for the electric polarizability anisotropy and related high-field properties are found for cylindrical and spherical geometries. Specific applications of the formulae are made for two systems; monodisperse DNA oligomers (involved in regulation of gene expression) and bovine disk membrane vesicles (vertebrate photoreceptor function).

Comparison experimental data on DNA oligomers can be found in the literature. The application includes the effects of both small and

large external electric fields. We also apply the model picture to spherical geometry and compute the equilibrium Kerr effect and compare it to the results of an experimental study of bovine disk membrane vesicles. Both systems permit the evaluation of the model parameters from other experiments and the comparison involves no adjustable fitting parameters. The dynamic Kerr effect response for disk membrane vesicles has been characterized and we anticipate an application of our model dynamics to the spherical geometry in the spirit of our previous work on cylinders.

2. Low-field Kerr effect – DNA

2.1. Determination of the anisotropy of polarizability

The calculation of the amplitude of the dipolar correlation function yields the magnitude of the low-field equilibrium Kerr effect as well.

The ratio of the low-field specific Kerr constant to its value extrapolated at infinite field allows cancellation of the optical anisotropy and yields the difference in electric polarizability (polarizability anisotropy) parallel and perpendicular to the long axis of the molecule ($\alpha_{\parallel} - \alpha_{\perp}$) [4].

For our case of a cylinder ($b = 1.3$ nm, L variable) the low-field electric polarizabilities ($\alpha_{\parallel}$, $\alpha_{\perp}$) are related to the amplitudes of the portions of the dipolar correction function (γ_z, γ_ϕ) via

$$m_{z'} = \alpha_{\parallel} E \approx \left\{ \int \cdots \int \prod_i \mathrm{d}z_i' \int \cdots \int \mathrm{d}\phi_i' e^2 L^2 E / k_B T \times \left[\sum (w_i - 1/2) \right]^2 \exp(-V'/k_B T) \right\} \times \left\{ \int \cdots \int \prod_i \mathrm{d}z_i' \int \cdots \int \mathrm{d}\phi_i' \times \exp(-V'/k_B T) \right\}^{-1} = e^2 L^2 E \gamma_z / k_B T \quad (1)$$

$$m_{\phi} = \alpha_{\perp} E \approx \left(e^2 b^2 E / 2 k_B T \right) \times \left\{ \int \cdots \int \prod_i \mathrm{d}z_i' \int \cdots \int \prod_i \mathrm{d}\phi_i' \times \left[\left(\sum \cos \phi_i' \right)^2 + \left(\sum \sin \phi_i' \right)^2 \right] \times \exp(-V'/k_B T) \right\} \times \left\{ \int \cdots \int \prod_i \mathrm{d}z_i' \int \cdots \int \mathrm{d}\phi_i' \times \exp(-V'/k_B T) \right\}^{-1} = e^2 b^2 E \gamma_\phi / 2 k_B T \quad (2)$$

where e is the electron charge, k_B Boltzmann's constant, E the Maxwell field parallel or perpendicular to the long axis, respectively, and V' contains the interactions between charged particles (and fixed charges if present). z', ϕ' and b are the molecule fixed cylindrical coordinates and $z' = wL$ ($0 \leqq w \leqq 1$).

The dipolar correlation function is

$$\gamma = \langle \vec{\mu}(t) \cdot \vec{\mu}(0) \rangle = e^2 L^2 \gamma_z + e^2 b^2 \gamma_\phi \quad (3)$$

Eqs. 1 and 2 are leading terms in a high-temperature expansion; this restricts their use to small external fields and allows their calculation from the components of the dipolar correlation function. We computed a few polarizabilities by both routes and found consistency as expected. The relation (used below) between the computed polarizability anisotropy and the amplitude of the equilibrium Kerr effect rests on the assumption that the polarizabilities along the molecular axes are not influenced by the orientation of the cylinder in space. This is clearly correct for small fields as it corresponds to a higher order in the high-temperature expansion.

Three different forms were used for V'. In the first no auxiliary charges are present and V' consists of the Coulombic repulsions between the counterions

$$V_1' = \sum_{j<i} \sum_i e^2 / 4\pi\epsilon\epsilon_0 |\vec{r}_i - \vec{r}_j| \quad (4)$$

where ϵ is taken to be the relative permittivity of water (78.45 at 25°C).

The second form for V' models the phosphates as a discrete set of negative charges along the axis of the cylinder. The number of these charges

equals the number of the phosphates (n) for the given length. The counterions interact (attractively) with the potential of the line charge. The first and second forms for V' would yield the same results for an infinitely long cylinder and their difference reflects end effects.

$$V_2' = V_1' + \sum_{i=1}^{n'} \sum_{j=1}^{n} -e^2/4\pi\epsilon\epsilon_0 k_B T|\vec{r}_i - \vec{r}_j| \qquad (5)$$

The third, and most realistic, potential models the phosphates as point charges on an idealized double helix (3.4 nm/turn) 1.0 nm away from the cylinder axis.

The calculation is made as a function of L, n' the number of counterions constrained to the surface of the cylinder, and the temperature T. To compare with experimental results on restriction fragments of DNA, we need an estimate of n'; n' is taken to be 0.76-times the number of phosphates (the 'condensation' model estimate) [5,6]. The question of the counterion distribution in the vicinity of the surface of rod-like DNA has been explored in detail recently [7]. The work of ref. 7 provides a comparison of the condensation model picture (two-phase approximation) with Poisson-Boltzmann and Monte Carlo calculations of counterion radial distributions. Although the two-phase counterion condensation model matches the other distributions only approximately, the model is successful in explaining thermodynamic properties.

We compare our calculations with the experimental determinations of the low-field equilibrium Kerr effect on DNA restriction fragments [8,9] and a related study of electric dichroism [10] which also yields the anisotropy of polarizability. Studies of DNA which are convoluted by an unknown molecular weight distribution are not considered [11–13].

A plot of $\log(\Delta\alpha)(\Delta\alpha = \alpha_{\parallel} - \alpha_{\perp}$, units C m^2 V^{-1}) vs. $\log L$ (L in m) is shown in fig. 1. The three model predictions are shown along with the data from refs. 8–10. Experimental points are shown for sample lengths up to about the persistence length of DNA [14] of about 45 nm. For longer samples, the molecules begin to form coils, the anisotropy of polarizability grows more slowly,

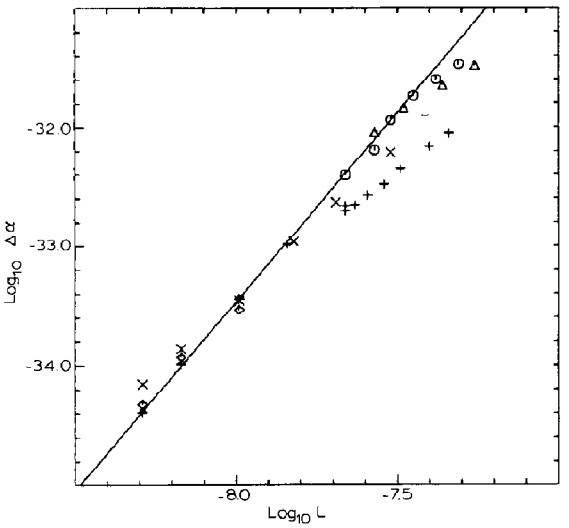

Fig. 1. Polarizability anisotropy of DNA oligomers as a function of length. Calculations 25°C: (×) No charge, (diamonds) line charge, (small triangles) helical charge. Experimental data: (circles) ref. 8, (large triangles) ref. 9, (+) ref. 10. The solid line is a least-squares fit to the helical charge data.

and the rod-like picture is inappropriate. Another presentation of the data is in table 1 where the anisotropy of polarizability has been divided by L^2 to suppress some of the dependence on length.

2.2. Temperature dependence

Changing the temperature affects the calculation of the polarizabilities ($\alpha_{\parallel}$, $\alpha_{\perp}$) through the influence of two reduced variables E/k_BT and V'/k_BT. Reducing the temperature makes a fixed field E more effective in inducing dipole moments since the randomizing thermal forces are relatively weaker and both $\alpha_{\parallel}$ and $\alpha_{\perp}$ increase as shown by the explicit temperature dependence in eqs. 1 and 2. The variable V'/k_BT influences the calculation of the components of the dipolar correlation function γ_z and γ_ϕ. Lowering the temperature enhances the role of Coulombic interactions. This makes the production of asymmetric counterion configurations more difficult and results in lower values for γ_z and γ_ϕ. The effect of temperature on γ_z and γ_ϕ can be seen in the data of table 2 for $L = 5.1$ nm (similar behavior is found for other values of L). Neither effect of E/k_BT or V'/k_BT

Table 1

$\Delta\alpha/L^2$ as a function of L

Units $C/V \times 10^{18}$ and nm, respectively.

No charge (5°C)		No charge (25°C)		Line charge (25°C)		Helical charge (25°C)	
$\Delta\alpha/L^2$	L	$\Delta\alpha/L^2$	L	$\Delta\alpha/L^2$	L	$\Delta\alpha/L^2$	L
2.77	5.1	2.68	5.1	1.82	5.1	1.55	5.1
3.12	6.8	2.97	6.8	2.54	6.8	2.23	6.8
		3.43	10.2	2.85	10.2	3.43	10.2
		4.73	15.3				
		5.61	20.4				
		6.66	30.6				
Ref. 8	(4°C)	Ref. 9	(20°C)	Ref. 10	(20°C)		
8.45	21.76	12.31	27.20	4.91	14.62		
8.70	27.20	13.01	33.32	4.27	21.76		
12.62	30.26	11.55	43.86	4.63	21.76		
14.66	35.36	11.12	54.74	4.05	23.46		
14.31	42.16	(1.97)	213.4	4.03	25.84		
14.03	49.30			4.11	28.56		
(11.23)	63.92			4.31	32.30		
(11.06)	72.42			4.29	40.12		
(10.69)	79.56			4.26	45.56		
(9.11)	90.78						
(4.10)	199.6						

is particularly large and they offset somewhat in the calculation of $\Delta\alpha$ (see table 1). The small effect of temperature is swamped by other factors and we do not attempt to bring the model calculations and the experimental data to a common temperature to enhance the comparison.

2.3. Dependence on the number of counterions

The dependence of γ_z and γ_ϕ on n' has been discussed previously [1,3]. For given L as n' increases, γ_z and γ_ϕ increase to a plateau value (and ultimately decrease, although this last behavior is not amenable to computation for technical reasons). For $V' = 0$ (no interactions), $\gamma_z = n'/12$ and $\gamma_\phi = n'$. Even for small n' large departures from the limiting case are found (see table 2) showing the significant role of the Coulomb forces in shaping the equilibrium Kerr effect and the dielectric increment. From our point of view the value of n' for DNA is determined by the choice of L ($L/0.17$ is the number of phosphates)

$$n' = 0.76L/0.17 \qquad (6)$$

The values of γ_z and γ_ϕ used to generate the data of table 1 are found from the γ_z (γ_ϕ) vs. n' curves for the predetermined values for n' (see appendix A).

2.4. Dependence on length

The literature abounds with theories of the dependence of $\Delta\alpha$ on L (equivalently the dielectric increments as a function of L) for rod-like biopolymers. No consensus exists and the quality of experimental data (particularly when convoluted by an unknown distribution of L) has precluded a critical comparison. Some of the theories were described in ref. 1 in connection with a discussion of the dielectric increment. Different predictions are L^3 dependence of $\Delta\alpha$ [15–18], L^2 dependence [19], $L^{3/2}$ dependence [20], and variable L dependence depending on the values of model parameters [21–23].

Our model has explicit L^2 dependence for $\alpha_\parallel$ and no explicit L dependence of $\alpha_\perp$. Implicit dependence on L occurs in the evaluation of γ_z and γ_ϕ. Since $\gamma_\parallel$ dominates $\Delta\alpha$ (particularly for

Table 2

Components of the dipolar correlation function

n'	$L = 5.1$ nm (25°C)		$L = 5.1$ nm (5°C) no charge	
	γ_z	γ_ϕ	γ_z	γ_ϕ
1	0.083	1.00	0.083	1.00
2	0.156	1.85	0.155	1.85
3	0.218	2.59	0.216	2.57
4	0.272	3.24	0.269	3.20
5	0.318	3.78	0.315	3.73
6	0.361	4.28	0.355	4.21
7	0.397	4.71	0.384	4.62
8	0.431	5.08	0.421	4.97
9	0.459	5.42	0.448	5.29
10	0.483	5.73	0.473	5.60
15	0.582	6.87	0.570	6.66
20	0.653	7.57		

n'	$L = 5.1$ nm (25°C)		$L = 6.8$ nm (25°C)			$L = 10.2$ nm (25°C) helical charge		
	γ_z	γ_ϕ	n'	γ_z	γ_ϕ	n'	γ_z	γ_ϕ
1	0.037	1.00	5	0.148	3.65	10	0.23	6.54
2	0.073	1.80	10	0.27	5.6	20	0.42	8.94
3	0.106	2.44	15	0.38	6.9	30	0.55	13.6
4	0.139	3.01	20	0.45	8.1	40	0.61	15
5	0.173	3.56	25	0.48	9.1	50	0.73	17
6	0.200	3.98	30	0.56	10.3			
7	0.229	4.36	32	0.58	12.4			
8	–	4.68						
9	0.280	4.97						
10	0.304	5.35						
11	0.331	5.55						
12	0.354	5.85						
14	0.395	6.40						
20	0.487	7.63						
23	0.53	8.7						

large L) and γ_z increases with L (via the concomitant increase in n'), over a small range of L an exponent of between 2 and 3 will be found. One can fit straight lines through the calculated points in fig. 1 and the slopes on the log-log plot are 2.51 ± 0.05 (no charge) and 3.2 ± 0.4 (helical charge).

The constancy of $\Delta\alpha/L^2$ for the experimental

Table 3

Effect of auxiliary charges on the dipolar correlation function (25°C)

n'	L (nm)	Helical charge		Line charge		No charge	
		γ_z	γ_ϕ	γ_z	γ_ϕ	γ_z	γ_ϕ
22.8	5.1	0.526	8.51	0.53	7.34	0.684	7.80
30.4	6.8	0.56	11.1	0.59	10.0	0.654	9.74
45.6	10.2	0.68	16	0.6	17.7	0.67	14.3

data in refs. 9 and 10 (see table 1) led to the conclusion of L^2 dependence whereas the data of ref. 8 approximate an L^3 variation.

2.5. The influence of fixed charges

Imposition of the helical configuration of negative charges tends to drive a similar helical configuration of the condensed counterions. This configuration has zero dipole moment in both the z' and ϕ directions and we expect γ_z and γ_ϕ to be less than the values of the dipolar correlation function components found for no charge. The effect is seen in the data of table 2 and is fairly pronounced, particularly for γ_z and small n'. γ_ϕ is not affected greatly and the differences in γ_z are reduced when L increases. The influence on L on γ_z can be seen in table 3 and a similar influence of L on $\Delta\alpha$ in table 1.

The comparison of $\Delta\alpha$ as a function of L is shown in table 1 and the data are plotted in fig. 1. The model results with the auxiliary helical charge distribution extrapolates into the experimental Kerr effect data [8,9]. The extrapolated curve and the Kerr effect data are 2–3 times the anisotropy of polarizability derived from electric dichroism (ref. 10, see table 1). We consider this comparison a success as there are no adjustable fitting parameters. Computational limitations preclude extending the model calculation into the experimental range of L; we hope to stimulate experimental measurements on shorter DNA oligomers so that a direct overlap of theory and experiment occurs.

Apart from random errors in the calculations and experiments, some uncharacterized systematic effects play a significant role.

The experimental Kerr effect results are not corrected for the internal field effect (ratio of the applied field to the Maxwell field). This factor scales the experimental values of $\Delta\alpha$. Unfortunately, the internal field correction for nonlinear electric fields is a matter of controversy in the literature and the correction could be as large as a factor of 2 [24].

In addition there is a role of added salt on the experiments (the model calculations are for no added salt). This question has been addressed [8,9,25]. It appears that the amount of added salt in the experiments quoted here is fairly low and should not invalidate the comparison (1 mM Na^+ [8], 0.1 mM Na^+ [9], 3 mM Na^+ [10]).

3. The saturating dipole

Outside the low-field regime the equilibrium Kerr effect is conveniently described in terms of the orientation function Φ.

$$\Phi = \langle P_2(\cos\theta)\rangle \tag{7}$$

which gives the fraction of the maximum specific Kerr constant which develops for a given electric field E.

Much discussion appears in the literature concerning the mechanism for the Kerr effect of rod-like polyelectrolytes. A consensus view is that an induced dipole mechanism operates at low fields and a permanent dipole mechanism explains the high-field response. This picture was made quantitative by Yoshioka [26] who neglected the transverse (ϕ) induced dipole moment and used the form (containing two adjustable parameters) (E along the molecular z' axis)

$$\begin{aligned} m_{z'} &= \alpha E \quad E \leq E_0 \\ &= m_s \quad E \geq E_0 \end{aligned} \tag{8}$$

A similar expression was used [10] to explain the field dependence of the electric dichroism. The algebra in going from eq. 8 to eq. 7 appears in ref. 26.

Our model allows the computation of Φ and $m_{z'}$ as a function of E without recourse to fitting parameters. The assumption (which we reject) behind eq. 8 is that all molecules contribute the same induced moment for a given field strength along the long axis. In fact, the $m_{z'}(E)$ function depends on the coordinates of the counterions $\{z_i', \phi_i'\}$ and one should average over the canonical ensemble distribution of configurations of the counterions to find the average polarizability α. For low fields α (i.e., $\alpha_\parallel$ to fit the picture of ref. 26) is constant and is given by eq. 1. Thus, data such as those in table 2 may be used to compute α for a choice of L, n' and temperature. The maximum dipole m_s which can develop in the molecule

fixed z' direction is $n'eL/2$. Thus

$$E_0 = n'k_B T/2eL\gamma_z \tag{9}$$

E_0 and α are functions of L, n' and γ_z. The $m_z'(E)$ function derived from eq. 1 shows a transition from the low-field to high-field behavior instead of the sharp break of eq. 8.

An analysis in a similar vein which allows comparison with the high-field equilibrium results of ref. 9 is to calculate the moment induced (per DNA molecule) in the direction of the Maxwell field. This involves additional averaging over the angles θ and ϕ between the long axis of the DNA and the Maxwell field (the third Euler angle is suppressed by symmetry). We construct a function in the spirit of eq. 8

$$\begin{aligned} m_z &= \alpha E \quad E \leqq E_b \\ &= m_{max} \quad E \geqq E_b \end{aligned} \tag{10}$$

Here the low-field response yields

$$\alpha = \left(e^2L^2\gamma_z + e^2b^2\gamma_\phi\right)/3k_BT \tag{11}$$

$$m_{max} = n'e\{b^2 + L^2\}^{1/2}/2 \tag{12}$$

$$E_b = 3n'k_BT\{b^2 + L^2\}^{1/2}/2e\left(L^2\gamma_z + b^2\gamma_\phi\right) \tag{13}$$

The actual m_z vs. E curve follows the function given in eq. 10 at low fields, rises above it at moderate fields ($E < E_b$), goes below the function in a range of field strengths around E_b, and finally becomes constant.

Some calculations of m_z (see the appendix) (no fixed charges on the cylinder) for $L = 10.2$ nm, $t = 25°C$ and $n' = 2$, 20 and 40 (E variable) are shown in table 4 and are plotted for $n' = 20$ (along with the function given by eq. 10) in fig. 2. It can be seen from this figure that the calculated data approximate the model function reasonably especially for small n'. The data of table 4 show that as n' increases, the break is less pronounced in the transition region from the 'induced dipole mechanism' to the 'permanent dipole mechanism'. As n' increases, the maximum dipole is more difficult to achieve as the Coulomb forces prevent the counterions from accumulating in the same region of configuration space. In fact, it seems that a quasi-plateau value of the induced moment occurs, the plateau value decreasing as n' increases. This behavior is similar to the n' dependence of the components of the dipolar correlation function.

Table 4

The induced moment as a function of field – DNA

$L = 10.2$ nm, $t = 25°C$, $f = m_z/m_{max}$.

E (V/m)	m_z/m_{max} ($n' = 2$)	m_z/m_{max} ($n' = 20$)	m_z/m_{max} ($n' = 40$)
10^6	0.0245	0.0109	
2×10^6	0.0491	0.0223	
3×10^6	0.0742	0.0347	
5×10^6	0.1253	0.0652	0.02
7×10^6	0.1780	0.106	0.04
10^7	0.2647	0.189	0.11
2×10^7	0.5497	0.424	0.24
3×10^7	0.7206	0.476	
5×10^7	0.8475	0.49	
7×10^7	0.8960	0.49	
10^8	0.9325	0.5	
2×10^8	0.9719		
3×10^8	0.9865		
5×10^8	0.9976		

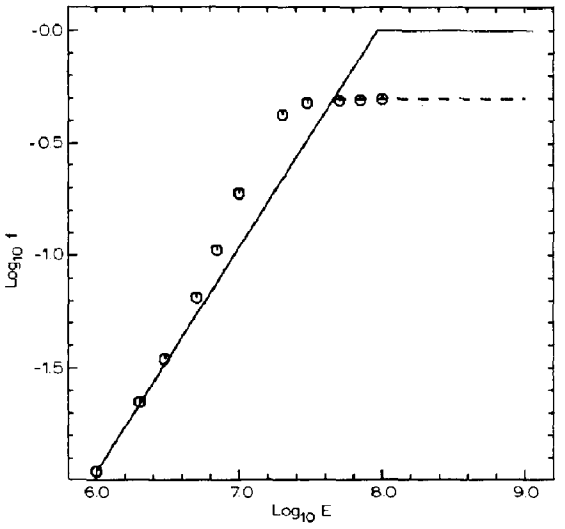

Fig. 2. Fraction f of the maximum dipole induced as a function of the Maxwell field for a DNA oligomer with length 10.2 nm. The solid lines are a plot of eq. 10 ($n' = 20$). The circles are the result of Monte Carlo calculations with $n' = 20$ and $t = 25°C$.

The plateau value might be used instead of the maximum value in eqs. 8 and 12.

The increase of m_z above the prediction of eq. 10 (α constant) results from the preferential occurrence of configurations with large dipole moments (along z') which are oriented along z as well. For small fields this coupling of internal and orientational coordinates is effectively absent; it becomes more important as the field strength increases. However, m_z must drop below the $\alpha =$ constant line at higher fields since m_z must be less than m_{max} and the limit is approached from below.

In ref. 9 a threshold field strength, E_{th}, at which the "rise of the birefringence becomes faster than the decay..." and "the Kerr law behavior was no longer obeyed" is reported as a function of the number of base-pairs (i.e., L) of the DNA oligomer. An inverse relationship fits the data. In terms of our picture E_{th} corresponds to the points at which the linear relationship between m_z and E fails; this is considerably less than E_b.

E_b shows approximate inverse dependence on L for the independent particle model ($V' = 0$). If $V' = 0$, $\gamma_z = n'/12$ and $\gamma_\phi = n'$. For $L \gg b$

$$E_b \approx 18 k_B T/eL \tag{14}$$

The slope of a plot of E_b vs. L^{-1} is 4.62×10^{-1} V. This compares to the corresponding slope [9] of 3.98×10^{-2} V for E_{th} vs. L^{-1}. This discrepancy is not surprising as the independent particle model is a poor picture of the molecular behavior and E_{th} and E_b are not directly comparable. From fig. 2 we would assign E_{th} to the value of E at which departures from the line $m_z = \alpha E$ of eq. 10 become significant. This occurs about an order of magnitude below E_b. For $n' = 45.6$ and $L = 10.2$ nm using eq. 13 and table 2 we find (helical charge) $E_b = 1.85 \times 10^8$ V/m. From the data of ref. 9 we find $E_{th} = 3.9 \times 10^6$ V/m. The displacement $\log E_{th}/E_b = -1.68$ is reasonable in the light of fig. 2. For $L = 5.1$ nm we find $E_b = 1.64 \times 10^8$ V/m and $E_{th} = 7.8 \times 10^6$ V/m. The displacement is -1.32. The dependence of E_b on L for our model is clearly weaker than L^{-1}. However, apart from the difference between E_B and E_{th}, our calculations are for relatively short DNA oligomers and the transverse dipole (γ_ϕ) plays a significant role whereas the data of ref. 9 are for longer molecules where the influence of displacements in the ϕ' direction is reduced.

4. Kerr effect – disk membrane vesicles

4.1. Disk membrane vesicles

The equilibrium (and dynamic) Kerr effect of photoreceptor disk membrane vesicles has been examined by Yu and co-workers [27,28]. When the vesicles are osmotically swollen in hypotonic media, one obtains a dilute aqueous suspension of monodisperse vesicles ($r = 4.7 \times 10^{-7}$ nm) with mobile charged species (rhodopsin) constrained to motion on the surface of the sphere (spherical shell). The motion is further constrained by the presence of a rim about the equator of the vesicle; half the charges are located on each hemisphere. The rim maintains the disk shape of the unswollen membranes when they are stacked in the rod outer segment [28]. The presence of the rim is deduced from the preservation of the semi-major axis of the series of oblate spheroids formed as the membrane is osmotically swollen from the disk to sphere shape [29]. In addition, the disk edge is thicker than the rest of the disk [30]. The rim confines the rhodopsin to its own hemisphere and has been identified as the source of the electrical anisotropy [28]. Our model of interacting diffusing charges on a surface can be applied to the spherical geometry (with and without the constraint of the rim) and we generate a prediction (without fitting parameters) for the equilibrium electrical polarizability anisotropy (and orientation function) as a function of the Maxwell field strength.

4.2. Working equations

The Kerr effect experiment determines the optical phase shift as a function of external field. The ratio of the phase shift to its limiting value at high field is the orientation function Φ (see eq. 7), P_2 is the second-order Legendre polynomial and θ is the angle between the laboratory z axis (applied field direction) and a specified symmetry axis of the solute molecule. According to the classical

theory [4,31,32], the solute is characterized by an intrinsic dipole moment μ and a polarizability anisotropy $\Delta\alpha$ which define phenomenological fitting parameters β, γ

$$\beta = \mu E/k_B T; \quad \gamma = \Delta\alpha E^2/2k_B T \tag{15}$$

where E is the Maxwell field. To apply the classical theory $\Phi(E)$ is fitted to eq. 7 using constant values of β and γ. The data for bovine disk membrane vesicles do not fit this model satisfactorily (H. Yu, personal communication).

A sphere with mobile surface charges and (possibly) symmetrically located fixed charges has no intrinsic dipole moment μ. To find γ we compute the polarizability (as a function of field strength) parallel and perpendicular to the plane of the rim (the former is larger). In the absence of the rim $\Delta\alpha = 0$ and the spheres would have no tendency to orient in an external field.

$$m_{\parallel} = \left\{ \int \cdots \int \prod_i \sin\theta_i \, d\theta_i \, d\phi_i [\ ] \exp[qerE[\ ]/k_B T - V'/k_B T] \right\} \times \left\{ \int \cdots \int \prod_i \sin\theta_i \, d\theta_i \, d\phi_i \exp[qerE[\ ]/k_B T - V'/k_B T] \right\}^{-1} \tag{16}$$

where

$$[\ ] = \sum_i \sin\theta_i \sin\phi_i \tag{17}$$

Similarly, for the calculation of $m_{\perp} = \alpha_{\perp} E$ via eq. 16 we have

$$[\ ] = \sum_i \cos\theta_i \tag{18}$$

$\{\theta_i, \phi_i\}$ are the coordinates of the mobile charges, n' the number of mobile charges, and qe the charge on the mobile species. E is the Maxwell field along the chosen molecular axis. $m_{\parallel}$ and $m_{\perp}$ are in units of qer. The multiplicity of the integral is determined by n' and the limits on the integral are different depending on the presence or absence of the rim. The potential V is composed of the field interaction $-\vec{\mu} \cdot E$ and V' the Coulombic repulsions between the mobile charges. The total mobile charge $n'q$ has been found to be 1.4×10^4 e [33] (H. Yu, personal communication). We see (below) that neglect of V' is justified and the vesicles orient nearly completely for small values of x

$$x = qerE/k_B T \tag{19}$$

Expanding the exponents and keeping the first nonvanishing term in the integrals yields

$$\alpha_{\parallel} = n'(qer)^2/3k_B T, \quad \alpha_{\perp} = n'(qer)^2/12k_B T,$$
$$\Delta\alpha = n'(qer)^2/4k_B T \tag{20}$$

Hence using eq. 15

$$\gamma = n'x^2/8 \tag{21}$$

A choice of q determines n' and leads to γ which allows calculation of Φ for the given field E.

We choose an inverted route to provide a comparison of theory with experiment. An observed value of Φ (with corresponding experimental applied field strength) yields γ. Given q, n' is found which yields x (see eq. 21). Eq. 19 is then used to find the model Maxwell field which generates the particular observed value of Φ. The experimental applied field E_{exp} and the model Maxwell field E_q may be compared. Differences resulting from internal field effects which are probably not representable by a constant factor (as in the classical theory [4]) are anticipated.

4.3. The induced dipole moment

In contrast to DNA oligomers which have a high surface density of counterion charges of 8.73 $\times 10^{-2}$ C/m^2, the bovine disk membrane vesicles have a charge density of only 9.81×10^{-4} C/m^2. In fig. 3 we show calculations of the fraction f of the maximum possible induced dipole moment ($n'qer$) for various values of n' and x. The data are tabulated in table 5. For (relatively) large fields (large x), f was determined by Monte Carlo integration with $n' = 32$ and $n' = 64$ (MC32, MC64). For (relatively) small fields (small x) f was calculated from a high-temperature expansion (ignoring V') with $n' = 16$ and $n' = 32$ (HT16,

HT32). For $n' = 2$ all coefficients in the high-temperature expansion were known exactly and the entire range of x could be spanned (HT2).

An examination of the data in table 5 shows that the MC and HT calculations yield the same results to within the accuracy of the computation, confirming our expectation that the V' term does not influence the calculation of f significantly. In addition the n' dependence of f is weak and has slowed by the time $n' = 64$ so that $f(x)$ does not depend on n'. This conclusion is supported by the data shown in fig. 3. For small x ($x < 1$), the high-temperature expansion can be terminated at the first nonvanishing term and we find $f = x/4$ strictly independent of n' (the proof requires $V' = 0$). The largest x value used for the comparison with experiment is $x = 0.07$. Also, we see from table 5 that the n' dependence of f is small for small x. It is easily shown that the curve HT2 is a lower bound for the other HT curves and lies below the MC results as well (this would be certain if V' were set equal to zero in the Monte Carlo calculations). Only moderate fields are needed to saturate the induced dipole moment.

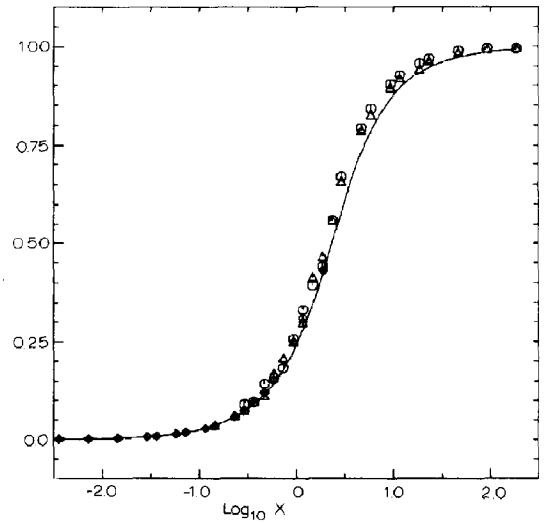

Fig. 3. Calculated fraction f of the maximum dipole induced as a function of the Maxwell field for disk membrane vesicles. High-temperature expansion: (curve) $n' = 2$, (diamonds) $n' = 16$, (+) $n' = 32$. Monte Carlo: (circles) $n' = 32$, (triangles) $n' = 64$.

For $f = 0.5$, $x = 0.31$ and for $q = 1$, $E = 1.7 \times 10^4$ V/m.

The presence of the rim reduces the moment which can be induced along the direction of the Maxwell field. With the rim we found $f = x/4$ for small x. Without the rim one has $f = x/3$. The difference reflects the increased configuration space available to the mobile charges when the rim is absent.

4.4. *The orientation function*

In ref. 34 the number of rhodopsins per vesicle was reported to be $n' = 7 \times 10^4$. If the total charge of the rhodopsins is taken as 1.4×10^4 e [35] (H. Yu, personal communication) we would have $q =$

Table 5

Saturation of the induced dipole moment – disk membrane vesicles

log x	MC64	MC32	HT32	HT16	HT2
−2.437	–	–	0.0009	0.0009	0.0009
−2.136	–	–	0.0018	0.0018	0.0018
−1.835	–	–	0.0037	0.0037	0.0037
−1.534	–	–	0.0073	0.0073	0.0073
−1.437	–	–	0.0092	0.0091	0.0091
−1.233	–	–	0.0146	0.0146	0.0146
−1.136	–	–	0.0183	0.0183	0.0183
−0.932	–	–	0.0294	0.0293	0.0292
−0.835	–	0.038	0.0368	0.0367	0.0365
−0.631	–	0.062	0.0594	0.0589	0.0584
−0.534	0.09	0.076	0.0749	0.0739	0.0729
−0.437	0.096	0.098	0.0946	–	0.0911
−0.330	0.144	0.113	0.124	0.120	0.1162
−0.233	0.160	0.170	0.158	0.152	0.1448
−0.136	0.184	0.210	–	–	0.1801
−0.029	0.257	0.251	–	0.250	0.2282
0.068	0.332	0.300	0.30	0.31	0.2814
0.165	0.393	0.413	–	–	0.3442
0.272	0.440	0.466	–	0.43	0.4241
0.369	0.560	0.562	–	–	0.5033
0.466	0.6689	0.6599	–	–	0.5837
0.670	0.7929	0.7874	–	–	0.7317
0.767	0.8412	0.8276	–	–	0.7853
0.971	0.9027	0.8955	–	–	0.8660
1.068	0.9263	0.9189	–	–	0.8929
1.272	0.9570	0.9434	–	–	0.9331
1.369	0.9697	0.9641	–	–	0.9465
1.670	0.9899	0.9857	–	–	0.9733
1.971	0.9950	0.9949	–	–	0.9866
2.272	0.9950	0.9969	–	–	0.9933

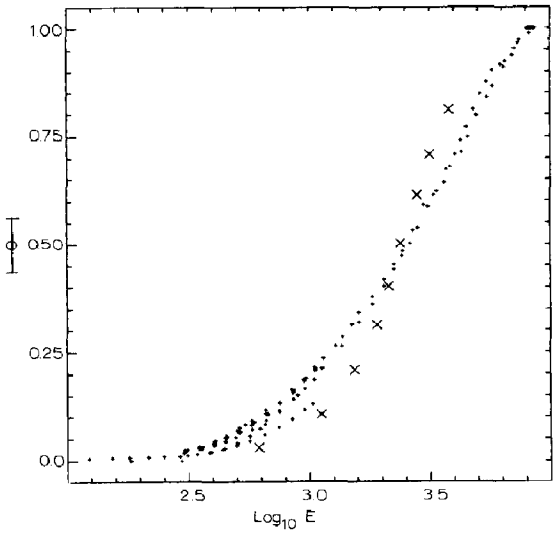

Fig. 4. Orientation function of disk membrane vesicles as a function of the Maxwell field. (+) Experimental data [13,14], (×) calculated values for $q = 1$ and $t = 25°C$.

0.2. These numbers are difficult to pin down and are subject to uncertainty. As an alternative we show the calculation with $n' = 1.4 \times 10^4$ and $q = 1$. A plot of Φ vs. log E_{exp} is shown in fig. 4. A few representative points are shown in table 6. From the experimental Φ values we calculate γ, x and the Maxwell E_q as described above. The ratio E_{exp}/E_q is shown for the two q values chosen and the points (Φ, $E_{q=1}$) are shown in fig. 4. From table 6 we see that the values of γ divided by E_{exp}^2 decrease markedly as E increases. Thus, it is no surprise that the classical theory ($\Delta\alpha$ fixed) fails to fit the data, even with μ (or β) added as an adjustable parameter. The model calculation, in which $\Delta\alpha$ is determined by averaging over configuration space, and varies with E, compares as well as could be expected considering uncertainties in assigning a value to q, the uncharacterized role of the internal field correction, and the neglect of counterions. With regard to the last point, in contrast to DNA, the counterions are much less strongly attracted to the biomacromolecule and their effect was ignored in the analysis of the electrooptic experiment [28].

5. Summary

The electrical polarizability anisotropy is calculated for rigid cylindrical polyelectrolytes as a function of the number of bound counterions (assumed to interact via Coulomb forces), length, temperature, and configuration of fixed polyelectrolyte charges. The result is used to calculate the amplitude of the low-field equilibrium Kerr effect. A comparison with data from the literature for DNA oligomers shows reasonable overlap between theory and experiment. For higher fields the formalism generates a 'saturating dipole' whose dependence on field strength is in qualitative agreement with experiment and mimics a proposed empirical function designed to fit equilibrium Kerr effect data for axially symmetric molecules in the saturating field regime.

Table 6

Field dependence of the orientation function

E in units of V/m.

ϕ	γ	E_{exp}	$E_{q=1}$	$E_{q=0.2}$	$E_{exp}/E_{q=1}$	$E_{exp}/E_{q=0.2}$
0.0302	0.2221	350	616	1380	0.57	0.25
0.1059	0.7472	668	1130	2530	0.59	0.26
0.2094	1.4281	1060	1560	3490	0.68	0.30
0.3128	2.1069	1500	1900	4240	0.79	0.35
0.4025	2.7289	2040	2160	4830	0.94	0.42
0.5022	3.4982	2630	2440	5470	1.07	0.48
0.6132	4.5958	3300	2800	6270	1.18	0.53
0.7089	5.9564	4250	3190	7130	1.33	0.60
0.8112	8.6734	4820	3850	8610	1.25	0.56

A parallel calculation was performed for spherical geometry. Here the focus is on calculating the induced dipole moment in an arbitrary strength electric field and on the orientation function. A comparison of the model prediction to the field strength dependence of the orientation function for bovine disk membrane vesicles was acceptable. The disk membrane vesicles have a special feature in that the bound charges are restricted to one or another of the hemispheres. In implementing the theory this shows up in the limits on the multiple integration in configuration space. The limits can be changed and the theory is applicable to spherical polyelectrolytes without the hemispherical constraint.

Appendix

A1. Evaluation of the dielectric increment

γ_z and γ_ϕ (see eqs. 1 and 2) were determined as a function of n' for the three choices of V′ and two temperatures by brute force Monte Carlo integration. The most time consuming calculations (helical charge) were executed on an IBM 3081 at the IBM Palo Alto Scientific Center. The remaining computations used a Vax 780 and a Harris/7. The correlation function components for the appropriate (fractional) condensation model estimates of n' were found by interpolation between calculated values or, in a few cases, by short extrapolation. Nonlinear regression of a fitting function consisting of a sum of a few exponentials was employed. The Metropolis scheme [36] proved inappropriate for the determination of γ_z and γ_ϕ due to the need to choose a very small maximum displacement for the counterion coordinates at each step.

A2. Evaluation of the saturating dipole – DNA

The working equation is

$$m_z = \left\{ \int \cdot \int \sin\theta \, d\theta \, d\phi \int \cdot \int \prod_i dz_i' \times \int \cdot \int \prod_i d\phi_i' [\ ] \times \exp\left([\ ] E/k_B T - V'/k_B T\right) \right\} \times \left\{ \int \cdot \int \sin\theta \, d\theta \, d\phi \int \cdot \int \prod_i dz_i' \times \int \cdot \int \prod_i d\phi_i' \times \exp\left([\ ] E/k_B T - V'/k_B T\right) \right\}^{-1} \quad \text{(A1)}$$

$$[\ ] = eL\Sigma\left(w_i - \tfrac{1}{2}\right)\cos\theta + eb\left(\Sigma \cos\phi_i \sin\theta \sin\phi + \Sigma \sin\phi_i \sin\theta \cos\phi\right) \quad \text{(A2)}$$

The scheme of section A1 was used. Calculations were done on a Vax 8600.

A3. Evaluation of the saturating dipole – disk membrane vesicles

The working equation is

$$m_z/qer = \left\{ \int \cdot \int \sin\theta \, d\theta \, d\phi \times \int \cdot \int \prod_i \sin\theta_i \, d\theta_i \, d\phi_i [\ ] \times \exp\left(qerE[\ ]/k_B T - V'/k_B T\right) \right\} \times \left\{ \int \cdot \int \sin\theta \, d\theta \, d\phi \times \int \cdot \int \prod_i \sin\theta_i \, d\theta_i \, d\phi_i \times \exp\left(qerE[\ ]/k_B T - V'/k_B T\right) \right\}^{-1} \quad \text{(A3)}$$

$$[\ ] = \cos\theta \, \Sigma \cos\theta_i + \sin\theta \sin\phi \, \Sigma \sin\theta_i \sin\phi_i + \sin\theta \cos\phi \, \Sigma \sin\theta_i \cos\phi_i \quad \text{(A4)}$$

To take advantage of the efficiency of the Metropolis algorithm [36], the θ_i, ϕ_i coordinates were restricted to 2592 discrete values (appropriately weighted by the associated area). A Metropolis Monte Carlo move consisted of an

attempt to move one particle (chosen randomly) to another cell. This procedure gave virtually the same answers as the brute-force full-configuration space procedure and converged much faster for large n'. As n' becomes large, the maximum induced dipole becomes slightly smaller than $n'qer$ and the entries in table 5 are the induced dipole divided by the actual maximum induced dipole. Calculations were performed on a Harris/7 computer.

For the high-temperature expansion the full continuous configuration space was used and eq. A3 employed to find the fraction f of the maximum induced dipole.

$$f = m_z/n'qer \tag{A5}$$

On expanding the exponentials in powers of x and neglecting V' we find

$$fn' = \frac{(x^1F(2,n')/1! + x^3F(4,n')/3! + ..)}{(x^0F(0,n')/0! + x^2F(2,n')/2! + ..)} \tag{A6}$$

The coefficients $F(p,n')$ are integrals over sums of products of trigonometric functions. Individual terms in the sums were related to tabulated integrals via regression relations. The bookkeeping was done on an IBM AT computer. The difficulty increased with the power of x and with n'. For $n' = 2$ we found

$$F(p,2) = 2p!/[(p/2+1)!]^2 \tag{A7}$$

and for $n' = 2$ the calculation could be carried to any order (the curve in fig. 3 includes terms up to $p = 300$).

For any n' the coefficients $F(p,n')$ were found to be power series in n' of degree $p/2$. Thus, a calculation of a finite number of terms for small n' ($p/2$ terms as the constant term is zero for $p > 0$) gave $F(p,n')$ for all n'. The scheme was implemented up to $p = 10$. A rearrangement of the power series (and expansion of the logarithm) yields

$$\ln F(p,n') = (p/2)\ln(p/2) + A + B/(n') + C/(n')^2 + .. \tag{A8}$$

where the coefficients of the expansion are determined in terms of the $p/2$ coefficients of the power series of $F(p,n')$. When all $p/2$ coefficients could not be calculated (due to computing limitations), eq. A8 was truncated at a point corresponding to the number of terms available. This was done up to $p = 28$. For $n' = 32$ this limits the convergence of the high-temperature expansion to $x < 2$.

Acknowledgements

This work was supported by the Research Committee of the University of Wisconsin-Madison and by a National Institutes of Health grant GM-0425. We thank H. Yu and M. Thomas Record, Jr for helpful discussions and H. Yu for access to the raw data of the Kerr effect of disk membrane vesicles. E.M. Turner and I. Rodriguez assisted with the calculations.

References

1 P.I. Meyer and W.E. Vaughan, Biophys. Chem. 12 (1980) 329.
2 P.I. Meyer, G.E. Wesenberg and W.E. Vaughan, Biophys. Chem. 13 (1981) 265.
3 G.E. Wesenberg and W.E. Vaughan, Biophys. Chem. 18 (1983) 381.
4 C.T. O'Konski, K. Yoshioka and W.H. Ortung, J. Phys. Chem. 63 (1959) 1558.
5 G.S. Manning, J. Chem. Phys. 51 (1969) 924.
6 J.W. Klein and B.R. Ware, J. Chem. Phys. 80 (1984) 1334.
7 P. Mills, C.F. Anderson and M.T. Record, Jr, J. Phys. Chem. 89 (1985) 3984.
8 J.G. Elias and D. Eden, Macromolecules 14 (1981) 410.
9 N.C. Stellwagen, Biopolymers 20 (1981) 399.
10 S. Diekmann, W. Hillen, M. Jung, R.D. Wells and D. Pörschke, Biophys. Chem. 15 (1982) 157.
11 D.C. Rau and E. Charney, Biophys. Chem. 17 (1983) 35.
12 R.S. Wilkinson and G.B. Thurston, Biopolymers 15 (1976) 1555.
13 S. Sokerov and G. Weill, Biophys. Chem. 10 (1979) 161.
14 C.R. Cantor and P.R. Schimmel, Biophysical chemistry, part III (W.H. Freeman, San Francisco, 1980) p. 1033.
15 M. Mandel, Mol. Phys. 4 (1961) 489.
16 S. Takashima, Adv. Chem. Ser. 63 (1967) 232.
17 N. Ise, M. Eigen and G. Schwarz, Biopolymers 1 (1963) 343.
18 C. Hornick and G. Weill, Biopolymers 10 (1971) 2345.
19 M. Hogan, N. Dattagupta and D.M. Crothers, Proc. Natl. Acad. Sci. U.S.A. 75 (1978) 195.

20 M. Sakamoto, H. Kanda, H. Hayakawa and Y. Wada, Biopolymers 15 (1976) 879.
21 J.P. McTague and J.H. Gibbs, J. Chem. Phys. 44 (1966) 4295.
22 M. Fixman, J. Chem. Phys. 72 (1980) 5177.
23 M. Fixman, Macromolecules 13 (1980) 711.
24 T. Keyes and B.M. Ladanyi, Adv. Chem. Phys. 56 (1984) 411.
25 E. Charney, K. Yamaoka and G.S. Manning, Biophys. Chem. 11 (1980) 167.
26 K. Yoshioka, J. Chem. Phys. 79 (1983) 3482.
27 H. Takezoe and H. Yu, Biophys. Chem. 13 (1981) 49.
28 H. Takezoe and H. Yu, Biophys. Chem. 14 (1982) 205.
29 T. Norisuye and H. Yu, Biochim. Biophys. Acta 471 (1977) 436.
30 F.J. Sjoestrand and M. Kreman, J. Ultrastruct. Res. 65 (1978) 195.
31 H. Benoit, J. Chim. Phys. 49 (1952) 517.
32 H. Benoit, Ann. Phys. 6 (1951) 561.
33 T. Kitano, T. Chang, G.B. Caflish, D.M. Piatt and H. Yu, Biochemistry 22 (1983) 4019.
34 E.J. Amis, D.A. Davenport and H. Yu, Anal. Biochem. 114 (1981) 85.
35 T. Norisuye, W.F. Hoffman and H. Yu, Biochemistry 15 (1976) 5678.
36 N. Metropolis, A.W. Rosenbluth, A.H. Teller and E. Teller, J. Chem. Phys. 21 (1953) 1087.